

Cite this: *RSC Adv.*, 2015, 5, 18506Received 26th November 2014
Accepted 28th January 2015

DOI: 10.1039/c4ra15278f

www.rsc.org/advances

A dislocation core in titanium dioxide and its electronic structure

Rong Sun,^a Zhongchang Wang,^{*b} Naoya Shibata^a and Yuichi Ikuhara^{*abc}

Insulating titanium dioxide finds numerous technological applications where dislocations can have profound implications for its performances. Herein, by combining advanced electron microscopy with first-principles calculations, we provide a direct atomic-resolution imaging of the core structure of a dislocation in TiO₂, and predict that individual impurity-free dislocation shows electric conductivity in otherwise insulating TiO₂. Electronic structure calculations reveals that there appears a confinement of spin-polarized conducting states within the dislocation core in a spatially connected fashion, acting as conducting pathways. Finding the local property shift at the dislocation core opens an additional avenue for manipulating dislocations as well as advances our understanding on functionalities of TiO₂.

Introduction

In the quest to optimize material performances, effort is increasingly devoted to understanding how the line defects in crystal lattices such as dislocations can radically alter properties of materials. In some circumstances, the line defects can be ruinous and a suppression of them is definitely crucial, whereas in other cases, they can be applied to fabricate one-dimensional nanostructures in crystalline solids for dislocation-engineered devices.^{1–3} These impacts can be attributed to the fact that the unique structural features of dislocations cause translational discontinuity, which locally alter stoichiometry and electronic states. Particularly, the lattice discontinuity at the core creates an elastic stress field around dislocations, which interacts with those of the solutes to accommodate excess elastic energy and consequently trap solute atoms to the dislocation lines, forming the so-

called “Cottrell atmosphere”.^{4,5} Moreover, the dislocation lines can serve as rapid diffusion pathways for enhanced mass transport, so-called pipe diffusion, which enforces the infiltration of foreign atoms acting as dopants, thereby mediating property shift.^{6–8} All these dislocation behaviors, including dynamics and interactions of dislocations, rely critically on the specific atomic structure, local chemistry, and local electronic states of their cores.

Titanium dioxide (TiO₂) has been investigated extensively over the past decades, largely because it finds potential applications in a wide range of technological fields, including catalysis, photocatalysis, sensors, solar cells, waste remediation, and biocompatible materials.^{9–12} It is intrinsically an inert wide-band-gap (~3 eV) semiconductor, yet many of its applications can be activated by additional electrons that originate from the defect states in the forbidden band gap.^{13,14} These gap states can, in principle, be triggered by a number of structural defects such as dislocations. Understanding their origins is therefore critical to improve the functionalities of TiO₂ because dislocations are implicated in many applications.^{15,16} It has been reported that there occur dislocations on the {101}, {110} and {100} planes in rutile TiO₂.^{17–19} The plastic deformation in rutile TiO₂ takes place by activating all the four {101}⟨101̄⟩ slip systems in the (001) orientation and by activating only two of the four {101}⟨101̄⟩ and the {100}⟨010⟩ slip systems in the (100) orientation.²⁰ The dislocations have been confirmed to affect the electrical properties of TiO₂ single crystals²¹ and the ionic conductivity of polycrystalline TiO₂.²² However, the understanding of the interplay between structure and property is still extremely difficult to achieve because the general knowledge on atomic-scale structure of dislocations and the effect they have on TiO₂ properties is still far from developed. These points remain a mystery due to the complicity of the defect structure, the challenge of probing a specific dislocation, and the intricacy in extracting electronic information on dislocation cores, albeit that dislocations in TiO₂ is often suspected to modify its properties. Here, by combining C_s-corrected high-angle annular dark-field (HAADF),^{23,24} annular bright-field (ABF)^{25,26} scanning transmission electron microscopy (STEM), and electron energy-

^aInstitute of Engineering Innovation, The University of Tokyo, 2-11-16 Yayoi, Bunkyo-ku, Tokyo 113-8656, Japan. E-mail: ikuhara@sigma.t.u-tokyo.ac.jp

^bAdvanced Institute for Materials Research, Tohoku University, 2-1-1 Katahira, Aoba-ku, Sendai 980-8577, Japan. E-mail: zcwang@wpi-aimr.tohoku.ac.jp

^cNanostructures Research Laboratory, Japan Fine Ceramics Center, 2-4-1 Mutsuno, Atsuta, Nagoya 456-8587, Japan

loss spectroscopy (EELS),²⁷ we offer direct an atom-resolved imaging of a core structure of a commonly occurring $\langle 001 \rangle$ dislocation in TiO_2 bicrystals,²⁸ and predict, by density functional theory (DFT) calculations, that there are unexpected spin-polarized conducting states at the dislocation core in otherwise insulating TiO_2 , modifying remarkably electronic properties of TiO_2 .

Experimental and computational details

It is known that the $\langle 001 \rangle$ and $\langle 101 \rangle$ dislocations can be introduced into TiO_2 crystals.²⁹ However, the naturally or plastically introduced dislocations are usually wavy and it is not so straight to directly resolve their core structures at the edge-on condition by TEM. Here, we adopted the low angle tilt grain boundary in bicrystals, which contains a periodic array of straight edge dislocations, to directly observe the core structure of TiO_2 .^{30–32} In addition, all atomic columns could in principle be identified from the $[1\bar{1}0]$ direction. For these reasons, the $\langle 001 \rangle$ edge dislocation is selected as a model system. The TiO_2 bicrystals with a small tilt angle of $\theta = 5^\circ$ were fabricated by precisely joining two pristine single-crystal blocks of rutile TiO_2 (upper and lower blocks) of high purity within the bicrystallographic relationships $(110)[001]_{\text{upper}} \parallel (110)[001]_{\text{lower}}$. To prepare pre-designed bicrystals with an array of confined dislocations, two single crystals were first cut by 2.5° from the (110) plane of the TiO_2 single crystal, followed by the mechanical grinding and polishing of the contact planes to a mirror finish. The two revealed surfaces were bonded with $[001]$ direction of one crystal almost parallel to $[001]$ direction of the other by a small tilt angle of 5° ($2.5^\circ + 2.5^\circ$) under hot pressing at 1773 K for 10 h in air. Specimens for TEM and STEM imaging were prepared by cutting, grinding, dimpling and argon ion-beam thinning. HAADF and ABF images were taken using the C_s -corrected ARM-200FC (JEOL, Ltd.) electron microscope operated at 200 kV, which provides an unprecedented opportunity to probe structures with sub-ångström resolution. For the HAADF STEM imaging, a probe convergence angle of ~ 22 mrad and a detector with an inner semiangle of over 60 mrad were adopted. The ABF STEM images were observed with a detector of 12–24 mrad, and EELS spectra were recorded using the Gatan Enfina system equipped on the STEM with an energy resolution, at full-width of half-maximum, of ~ 0.5 eV.

Calculations were carried out using Vienna *ab initio* simulation package (VASP) within the DFT.³³ We applied the projector augmented wave method³⁴ with $1 \times 1 \times 7$ k -point grids and a cutoff energy of 400 eV, which enabled an accurate prediction of the atomic and electronic structures of the dislocation systems. The generalized gradient approximation (GGA) of Perdew *et al.*³⁵ (PW91) plus U -method was applied with $U = 4.5$ and $J = 1.0$ eV to address the Ti 3d orbitals. To simulate realistic dislocations, we imposed periodic boundary conditions along the dislocation-line ($[1\bar{1}0]$) and Burgers-vector ($\mathbf{b} = [001]$) direction and embedded a vacuum of 10 Å into the supercells along the $[110]$ direction to avoid unwanted interactions between dislocations. Dislocation cores were modeled with a

large periodic supercell containing up to 668 atoms using DFT, which were further adopted for image simulations. The optimum lattice constants of the rutile TiO_2 bulk calculated using this method were $a = 4.632$ Å and $c = 2.983$ Å, which are consistent with the reported experimental values.³⁶

Results and discussion

Structural characterization of the prepared bicrystal

To confirm the pre-designed orientation relationship of the bicrystal and clarify whether dislocations are introduced into the boundary area, we acquired the selected-area diffraction pattern (SADP) (Fig. 1(a)) and STEM image (Fig. 1(b)) of the boundary area in the 5° $[001]$ bicrystal, in which the incident electron beam is along the $[1\bar{1}0]$ direction. An overall symmetry is clearly seen in the pattern, and a slight yet visible splitting is revealed for some diffraction spots (Fig. 1(a)). In light of the splitting spots in the SADP, the misfit tilt angle (θ) of the bicrystal is estimated to be $\sim 5.1^\circ$, indicating a successful output of a bicrystal with the prescribed orientation relationships. As seen in Fig. 1(b), there emerges periodic image contrast exactly on the mirror plane of the $(110)[001]$ boundary (indicated by arrows), suggesting the confinement of an array of dislocations at the boundary. The dislocation core structures are expected to be observed at edge-on condition. The two crystals are well bonded with no secondary-phase layers, amorphous layers, contaminants, or transitional areas at the boundary region.

To offer atomic details, we show in Fig. 1(c) the HAADF STEM image of a representative dislocation viewed from the $[1\bar{1}0]$ direction. Because the intensity of an atomic column in the

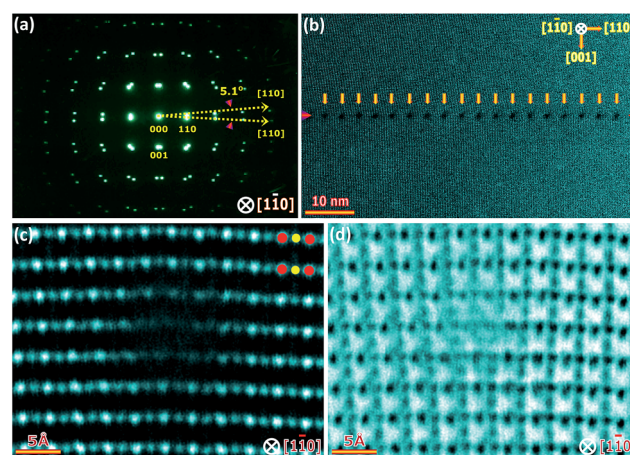


Fig. 1 (a) Selected-area diffraction pattern (SADP) taken at the boundary area. An overall symmetry is seen in the pattern, indicating a perfect joining of the two single crystals. (b) Low-magnification ADF STEM image of the boundary in the bicrystal, confirming the formation of a periodic array of dislocations at boundary, as indicated by arrows. (c) Atomic-resolution HAADF STEM image of a dislocation viewed from the $[1\bar{1}0]$ projection. The red circle indicates the Ti–O mixed column and the yellow one indicates the pure Ti column. It is noteworthy that many dislocations at different places have been explored and only one type of dislocation core has been detected. (d) The corresponding ABF STEM image recorded simultaneously with the HAADF image.

HAADF mode is directly proportional to $Z^{1.7}$ (Z : atomic number),³⁷ image contrast is brighter for heavier atoms and larger atomic density in the atomic columns. This means that lighter spots represent pure Ti columns (smaller circle), whereas brighter ones represent Ti–O mixed columns (larger circle), which unravels an almost symmetric core geometry for the edge dislocation of TiO_2 . We also performed atomic-resolution imaging of many other dislocations at the boundary region and found that all acquired images point to an identical core configuration. The core region is slightly darkened owing to the strain associated with the dislocation. In addition, the considerably lighter O atoms are not scattered strongly enough to be visualized. To complement the HAADF STEM image, we also conducted ABF STEM imaging of this dislocation, as shown in Fig. 1(d). The ABF STEM technique has been proven to allow a simultaneous imaging of light and heavy atoms with good signal-to-noise ratio, robustly over a range of sample thickness.^{25,26} Apart from extracting the same structural information as in HAADF, the ABF image, in which dark spots represent atomic columns, allows us to identify each individual oxygen column at the dislocation core.

To probe electronic structures of a single dislocation, we perform EELS analyses of the $\text{Ti-L}_{2,3}$ edge for the dislocation core region together with that of the bulk as a reference (Fig. 2). Evidently, the $\text{Ti-L}_{2,3}$ EELS spectrum in the region away from the dislocation core (close to the bulk) consists mainly of four peaks (*i.e.* two doublets), where one doublet at lower energy loss comprises the Ti-L_3 edge, whereas the other at the higher energy loss Ti-L_2 edge shows a characteristic of having a valence state of +4 for the Ti atoms away from the core.³⁸ In contrast, the $\text{Ti-L}_{2,3}$ EELS spectrum taken at the core area exhibits a broader profile (marked by arrows in Fig. 2), suggesting that they are of a mixed valence state of +3/+4 because the key difference in the $\text{Ti-L}_{2,3}$ EELS spectrum between Ti^{4+} and Ti^{3+} rests with the broadening of the t_{2g} peaks in each doublet. We further conducted EELS measurements over a broad energy span and find that only the signatures of $\text{Ti-L}_{2,3}$ and O-K edges are detected both at the core and in bulk, providing evidence that a substantial segregation of impurity to the core can be ruled out, *i.e.* the dislocation core is impurity free. Such a shift in electronic states indicates the formation of a conducting channel at an individual dislocation

and points to the existence of novel impacts associated with the impurity-free dislocations of TiO_2 .

Electronic structure of the dislocation

To gain insights into physical mechanism of the property shift associated with the dislocation and the quantum nature of the conducting states, we conduct DFT calculations using the generalized gradient approximation functional plus the on-site repulsion U -method. In light of the aforementioned orientation relationships and bulk structure of rutile TiO_2 , we constructed an atomic model based on the observed HAADF and ABF STEM images (Fig. 1(c) and (d)), followed by a structural relaxation (Fig. 3(a)). It is noteworthy that due to the nonstoichiometry of the dislocation and the embedded vacuum, we have not estimated the formation energy of this dislocation core. The atomistic model contains the typical expansion, intermediate, and compression areas. We further superimposed the model onto the observed ABF image, as shown in Fig. 3(b), and found that their overall features agree qualitatively with each other. The slight discrepancy can be attributed to the used limited supercell size.

Fig. 3(c)–(f) shows calculated electronic structure of the bulk (away from the core) and the core. It should be noted that the total density of states (DOS) is collected from those atoms around the core, *i.e.* the surface states originating from the embedded vacuum are not included. Our calculations confirm the insulating nature of the bulk: the Fermi level (E_F) lies in the gap between states in the DOS, splitting the filled O 2p from the unfilled Ti 3d orbitals, which indicates that the relaxed atomic model can be applied to represent the dislocation core, notwithstanding the slight discrepancy due to the limited supercell size. On the other hand, the electronic structure of the core differs remarkably from that of the bulk: the E_F shifts downward and eventually overlaps the tail of the valence band (VB) in the spin-minority channel, indicating a half metallicity. Moreover, a ferromagnetic alignment of spins is clearly observed: states occur at E_F in the spin-minority channel, whereas there are no states at E_F in the spin-majority channel, leading to gap opening. A significant hybridization is also seen between the Ti 3d and O 2p states at E_F , inducing a peak in the DOS for the O atoms at the core. Further analysis of the orbital contribution reveals that the filled Ti 3d states at E_F originate mainly from the d_{xz} states in the spin-minority channel (Fig. 3(f)), raising the likelihood that conducting channels may form along the dislocation line (z direction). Such spin polarization indicates that the Ti atoms at the core have a mixed valence state of +3/+4, which is consistent with the EELS data.

To gain insights into the spatial distribution of the spin-polarized conducting states and bonding nature of the dislocation, we present contour plots of charge density along the two orthogonal $[1\bar{1}0]$ and $[001]$ directions (Fig. 4). The majority of charges at E_F , which arise primarily from the interaction of the Ti 3d and O 2p states, are confined, to a large extent, to the core area (Fig. 4(a)), and this is consistent with the DOS analyses (Fig. 3). Furthermore, the charges localized on the O show humps distorted toward their neighboring Ti, suggesting that the bonds at the core have a mixed covalent–ionic character.

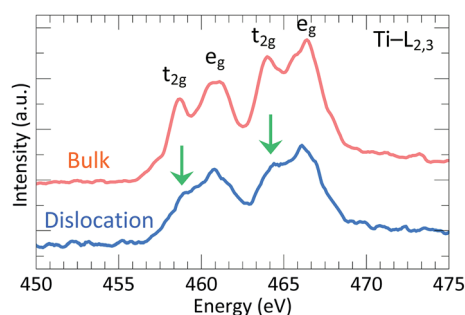


Fig. 2 The $\text{Ti-L}_{2,3}$ edge EELS profiles recorded at the dislocation core and in the bulk region (*i.e.* away from the core). The region used to represent the TiO_2 bulk is ~ 10 nm far from the exact dislocation core.

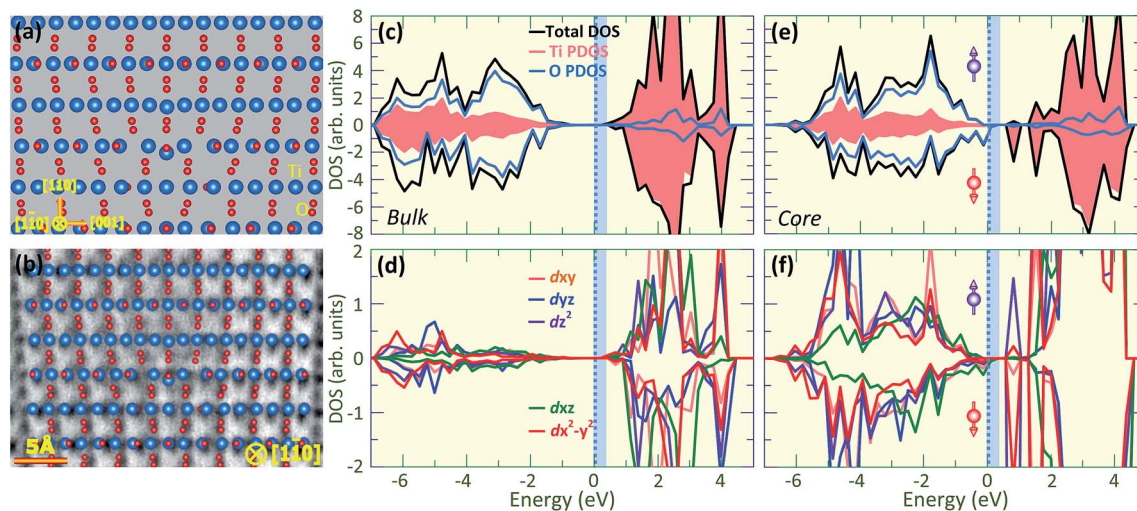


Fig. 3 (a) Relaxed atomic model of an edge dislocation with $\mathbf{b} = [001]$ viewed from the $[1\bar{1}0]$ projection. The model is constructed based on the experimental image. The larger balls are Ti atoms and the smaller ones are O atoms. (b) The fully optimized atomistic model superimposed on the ABF STEM image. The slight discrepancy can be attributed to the limited supercell size. Total and partial DOS (PDOS) plots of the Ti and O atom contributions for the (c) bulk and (e) dislocation core. The PDOS plots of the Ti 3d orbitals for the (d) bulk and (f) dislocation core. The E_F is set to zero.

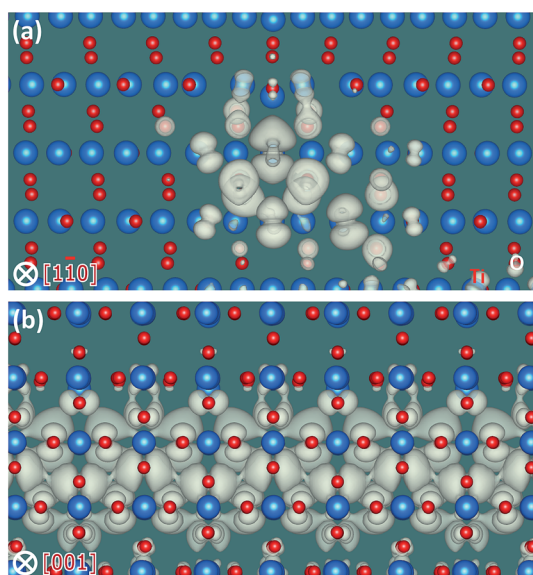


Fig. 4 Charge distribution in the dislocation system for the electronic states at E_F viewed along (a) $[1\bar{1}0]$ (dislocation-line) and (b) $[001]$ (Burgers-vector) directions. The big and small balls denote the Ti and O atoms, respectively.

Interestingly, the charges accumulated at the core are spatially connected along the dislocation line in a channel-like fashion (Fig. 4(b)), rendering each individual dislocation a potential pathway for enhanced electrical conductivity.³⁹

Conclusions

We have obtained a direct atom-resolved imaging of the core structure of the commonly occurring $\langle 001 \rangle$ dislocation in

technologically important TiO_2 and demonstrated that Ti atoms at the impurity-free dislocation core have a mixed valence state of +3/+4, indicating that each individual dislocation can serve as a conducting channel. Atomistic calculations predict that spin-polarized conducting states occur at E_F , and these states are confined to the dislocation core. This combined technique allows us to gain insights into the complex atomic structures and unusual physical properties of dislocation, which could be applicable to other types of defects.

Acknowledgements

This work was conducted in part at the Research Hub for the Advanced Nano Characterization and “Nanotechnology Platform” at Univ. of Tokyo supported by MEXT of Japan and was supported in part by the Elements Strategy Initiative for Structural Materials (ESISM) via MEXT by Japan and the JSPS Grant-in-Aid for the Scientific Research on Innovative Areas “Nano Informatics”. R.S. is supported by the MEXT scholarship. Z.C.W. acknowledges the financial support from the Grant-in-Aid for Young Scientists (A) (grant no. 24686069), NSFC (grant no. 11332013), JSPS and CAS under the Japan-China Scientific Cooperation Program, and Murata Science Foundation. N.S. acknowledges the support from JST-PRESTO and JSPS KAKENHI (grant no. 23686093). Calculations were conducted at ISSP, Univ. of Tokyo.

Notes and references

- 1 A. Nakamura, K. Matsunaga, J. Tohma, T. Yamamoto and Y. Ikuhara, *Nat. Mater.*, 2003, **2**, 453.
- 2 Y. Ikuhara, *Prog. Mater. Sci.*, 2009, **54**, 770.
- 3 I. Sugiyama, N. Shibata, Z. C. Wang, S. Kobayashi, T. Yamamoto and Y. Ikuhara, *Nat. Nanotechnol.*, 2013, **8**, 266.

- 4 A. H. Cottrell and B. A. Bilby, *Proc. Phys. Soc., London, Sect. A*, 1949, **62**, 49.
- 5 A. Kelly, W. R. Tyson and A. H. Cottrell, *Philos. Mag.*, 1967, **15**, 567.
- 6 T. Nakagawa, A. Nakamura, I. Sakaguchi, N. Shibata, K. P. D. Lagerlof, T. Yamamoto, H. Haneda and Y. Ikuhara, *J. Ceram. Soc. Jpn.*, 2006, **114**, 1013.
- 7 G. R. Love, *Acta Metall.*, 1964, **12**, 731.
- 8 M. Legros, G. Dehm, E. Arzt and T. J. Balk, *Science*, 2008, **319**, 1646.
- 9 M. S. Chen and D. W. Goodman, *Science*, 2004, **306**, 252.
- 10 X. B. Chen, L. Liu, P. Y. Yu and S. S. Mao, *Science*, 2011, **331**, 746.
- 11 J. A. Rodriguez, S. Ma, P. Liu, J. Hrbek, J. Evans and M. Pérez, *Science*, 2007, **318**, 1757.
- 12 L. J. Diguna, Q. Shen, J. Kobayashi and T. Toyoda, *Appl. Phys. Lett.*, 2007, **91**, 023116.
- 13 Y. Q. Gai, J. B. Li, S. S. Li, J. B. Xia and S. H. Wei, *Phys. Rev. Lett.*, 2009, **102**, 036402.
- 14 S. Wendt, P. T. Sprunger, E. Lira, G. K. H. Madsen, Z. S. Li, J. Hansen, J. Matthiesen, A. Blekinge-Rasmussen, E. Lagsgaard, B. Hammer and F. Besenbacher, *Science*, 2008, **320**, 17554.
- 15 Y. Nakano, T. Morikawa, T. Ohwaki and Y. Taga, *Appl. Phys. Lett.*, 2005, **87**, 052111.
- 16 H. S. Ahn, S. Han and C. S. Hwang, *Appl. Phys. Lett.*, 2007, **90**, 252908.
- 17 W. M. Hirthe and J. O. Brittain, *J. Am. Ceram. Soc.*, 1962, **45**, 546.
- 18 K. H. G. Ashbee and R. E. Smallman, *Proc. R. Soc. London, Ser. A*, 1963, **274**, 195.
- 19 H. Li and R. C. Bradt, *J. Am. Ceram. Soc.*, 1990, **73**, 1360.
- 20 S. Basu, O. A. Elshrief, R. Coward, B. Anasori and M. W. Barsoum, *J. Mater. Res.*, 2012, **27**, 53.
- 21 K. K. Adepalli, M. Kelsch, R. Merkle and J. Maier, *Adv. Funct. Mater.*, 2013, **23**, 1798.
- 22 K. K. Adepalli, M. Kelsch, R. Merkle and J. Maier, *Phys. Chem. Chem. Phys.*, 2014, **16**, 4942.
- 23 P. D. Nellist, M. F. Chisholm, N. Dellby, O. L. Krivanek, M. F. Murfitt, Z. S. Szilagyi, A. R. Lupini, A. Borisevich, W. H. Sides Jr and S. J. Pennycook, *Science*, 2004, **305**, 1741.
- 24 N. Shibata, M. F. Chisholm, A. Nakamura, S. J. Pennycook, T. Yamamoto and Y. Ikuhara, *Science*, 2007, **316**, 82.
- 25 S. D. Findlay, N. Shibata, H. Sawada, E. Okunishi, Y. Kondo, T. Yamamoto and Y. Ikuhara, *Appl. Phys. Lett.*, 2009, **95**, 191913.
- 26 S. D. Findlay, N. Shibata, H. Sawada, E. Okunishi, Y. Kondo and Y. Ikuhara, *Ultramicroscopy*, 2010, **110**, 903.
- 27 C. Colliex, *Nature*, 2007, **450**, 622.
- 28 A. Mebarek, A. Lemmoui and M. Beccouche, *Global J. Phys. Chem.*, 2011, **2**, 170.
- 29 K. Suzuki, M. Ichihara and S. Takeuchi, *Philos. Mag. A*, 1991, **63**, 657.
- 30 Y. Ikuhara, H. Nishimura, A. Nakamura, K. Matsunaga, T. Yamamoto and K. P. D. Lagerlof, *J. Am. Ceram. Soc.*, 2003, **86**, 595.
- 31 E. Tochigi, Y. Kezuka, N. Shibata, A. Nakamura and Y. Ikuhara, *Acta Mater.*, 2012, **60**, 1293.
- 32 E. Tochigi, N. Shibata, A. Nakamura, T. Mizoguchi, T. Yamamoto and Y. Ikuhara, *Acta Mater.*, 2010, **58**, 208.
- 33 G. Kresse and J. Hafner, *Phys. Rev. B: Condens. Matter Mater. Phys.*, 1993, **47**, 558.
- 34 P. E. Blöchl, *Phys. Rev. B: Condens. Matter Mater. Phys.*, 1994, **50**, 17953.
- 35 J. P. Perdew, J. A. Chevary, S. H. Vosko, K. A. Jackson, M. R. Pederson, D. J. Singh and C. Fiolhais, *Phys. Rev. B: Condens. Matter Mater. Phys.*, 1992, **46**, 6671.
- 36 S. Gemming, R. Janisch, M. Schreiber and N. A. Spaldin, *Phys. Rev. B: Condens. Matter Mater. Phys.*, 2007, **76**, 045204.
- 37 S. J. Pennycook and L. A. Boatner, *Nature*, 1988, **336**, 565.
- 38 E. Stoyanov, F. Langenhorst and G. Steinle-Neumann, *Am. Mineral.*, 2007, **92**, 577.
- 39 Z. C. Wang, S. Tsukimoto, M. Saito and Y. Ikuhara, *Appl. Phys. Lett.*, 2009, **95**, 184101.